ACS OMEGA

Open Access

http://pubs.acs.org/journal/acsodf

Article

Rapid Detection of Total Petroleum Hydrocarbons in Soil Using Advanced Fluorescence Imaging Techniques

Gaoyong Shi, Ruifang Yang,* Nanjing Zhao,* Gaofang Yin, Jinqiang Yang, Yuxi Jiang, and Wenqing Liu

Cite This: *ACS Omega* 2024, 9, 29350−29359

Read Online

ACCESS | Metrics & More | Article Recommendations | Supporting Information

ABSTRACT: Chemical methods for measuring soil organic content are often slow and yield inaccurate results due to significant errors. Simple summation of components may not accurately determine total organic content. In contrast, fluorescence imaging techniques offer rapid, in situ monitoring without complex pretreatment and demonstrate rapid and accurate assessment of soil organic content. Utilizing a soil organic pollutant fluorescence imaging in situ monitoring system that we independently developed, we conducted laboratory experiments to explore methods for acquiring fluorescence signals of petroleum hydrocarbons in soil and extracting image features. We used this monitoring system to obtain fluorescence images of crude oil in standard soil (soil properties are shown in Table S1) samples at concentrations ranging from 0 to 100 g/kg, and the coefficient of determination of the total amount inversion model reached 0.999. Simultaneously, we applied the system to a deserted petroleum storage area, and the relative standard deviation values of 16 of the 18 groups of tests were less than 1%, indicating that the monitoring system is highly stable when applied in the field. This study provides both theoretical foundation and technical support for the rapid and nondestructive detection of total petroleum hydrocarbons in soil at field sites.

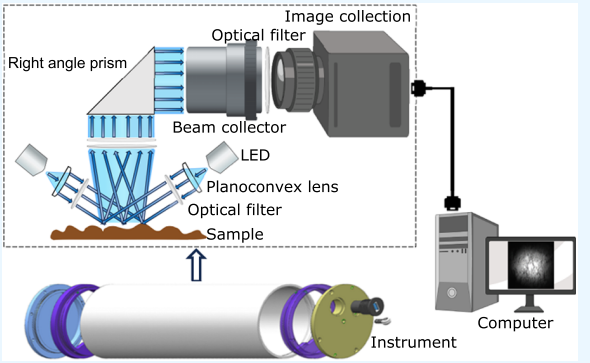

INTRODUCTION

In the past few decades, because of the rapid expansion of the cities and the implementation of the "Retreat from the city and enter the park" policy, many industrial enterprises in old urban areas have relocated to industrial parks, suburbs, and development zones. The original factories had to face the suspension of production and relocation. Therefore, when these lands need to be repurposed, soil quality[1] becomes the most concerning issue, especially the degree of contamination with polycyclic aromatic hydrocarbons (PAHs)[2] and petroleum hydrocarbons. As a result, it is critical to conduct pollution surveys on this type of land to improve our understanding of the pollution situation. This approach enables us to determine whether existing uses can be developed quickly. Due to the difficulty of natural degradation, polycyclic aromatic hydrocarbons and petroleum hydrocarbons have an increased potential to harm humans.[3] During the past few decades, many industrial parks in China have been affected by this issue. For example, after the relocation of a petrochemical company in the northern region,[4] excessive levels of benzene, toluene, ethylbenzene, total petroleum hydrocarbons, and other pollutants have been found in the soil at the initial site, and serious pollution resulted from this. After a gas station was relocated in Shanghai,[5] the total petroleum hydrocarbons in the soil samples were within standard limits, but the total petroleum hydrocarbons, lead, and benzene in the groundwater samples exceeded the standard limits. In 27 soil samples at different depths collected from the site of relocation of a machinery manufacturing company in Shijiazhuang,[6] two types of total petroleum hydrocarbons and three types of benzene series have been detected. However, no levels exceeded acceptable levels. The primary type of pollution at the original oil plant site is soil petroleum pollution. As oil pollutants enter the soil, they can be readily absorbed by soil-reactive surfaces, altering their physical, chemical, and biological properties.[7,8] Moreover, petroleum pollutants can also be transported and bioaccumulated in various media, posing serious threats to human health and the environment.[9] As an important reservoir and transfer station for petroleum hydrocarbons,[10] soil plays a crucial role in reclaiming contaminated sites. Rapid in situ monitoring of petroleum pollutants and remediation measures are essential for legacy site redevelopment.

Organic pollutants are primarily detected through laboratory analysis using gas chromatography, liquid chromatography, mass spectrometry, and combinations thereof.[11−15] These

Received: February 9, 2024
Revised: June 13, 2024
Accepted: June 14, 2024
Published: June 27, 2024

methods are mature and offer high sensitivity and accuracy. However, they require more complex sample pretreatment, and the extraction of PAHs poses some challenges due to their varied structures, ranging from two rings to six or more rings as shown in Figure 1. Therefore, it is necessary to develop

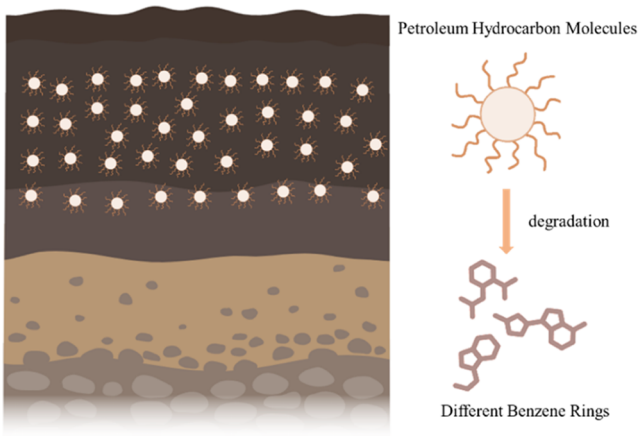

Figure 1. Soil of the oil plant area left behind after the relocation contains a large amount of petroleum hydrocarbon molecules. They can have many different structures ranging from two rings to six or more rings.

extraction methods adapted to the different types of PAHs.[16] Additionally, some PAHs are volatile, which means that if they are extracted and analyzed, they may be lost. Hence, certain measures must be taken to prevent errors resulting from this volatility.[17] Furthermore, traditional methods incur high analysis costs, hindering the dynamic monitoring needs of soil organic pollution. Thus, the development of a fast, convenient, and on-site method for detecting soil organic pollutants is beneficial for improving agricultural economic benefits and preserving soils for future generations. Three-dimensional fluorescence spectroscopy,[18] visible to near-infrared spectroscopy,[19] and hyperspectroscopy[20] are currently used for rapid, nondestructive quantitative detection of petroleum hydrocarbons in soil, but they are generally employed for detecting their components.

Recently, several emerging technologies, such as fluorescence imaging technology, have been applied to organic detection. The samples are detected and analyzed rapidly by monitoring their fluorescence signals to ensure that they are detected and quantified in real time. Hao et al.[21] had used a fluorescence hyperspectral imaging technique with an excitation wavelength of 357 nm to determine the amount of total polycyclic aromatic hydrocarbons in roasted lambs. They created a prediction model combining partial least-squares regression, a least-squares support vector machine, and convolutional neural networks. This model predicted the total polycyclic aromatic hydrocarbon content of roasted lambs with a coefficient of determination of 0.9011 and a root-mean-square error of 0.0179 mg/kg. Qazi et al.[22] had used confocal microscopy as a fast and accurate technique for detecting, identifying, and tracking naphthalene, phenanthrene, and pyrene through the inherent fluorescence of PAHs; then, direct analysis of soil samples revealed that up to 1 g/kg PAHs were detected in the soil samples. Wesley McCall et al.[23] had used a self-developed optical image profiler and ultraviolet light-emitting diodes to induce fluorescence in soil gasoline, diesel oil, and crude oil. The diesel and gasoline detection limits were 0.1 g/kg, while the crude oil detection limit was 0.05 g/kg. Both produced accurate log−linear responses. This method has several advantages, including its nondestructive nature, rapid response, and lack of complicated sample preparation and processing activities. This approach provides an opportunity to rapidly determine the total petroleum hydrocarbon content of soil on site. Cao et al.[24] had developed a method for detecting petroleum components and monitoring petroleum content in soil and groundwater using dual excitation Raman spectroscopy and microscopy. The extraction-Raman spectroscopy detection time was 0.5 h, and the fiber-Raman spectroscopy detection time was 1 min. The detection limit of soil petroleum hydrocarbons was 0.094 g/kg.

Compared with other studies, we used an area array CCD (charge-coupled device (CCD)) camera with small size, lightweight, low power consumption, and low operating voltage as a photodetector to detect fluorescence image signals. It has high resolution and sensitivity, fast detection speed, and real-time monitoring capabilities. For the obtained fluorescence images, we used the maximum interclass variance method to obtain the image threshold and calculated the mean gray value, which improved the accuracy and efficiency of soil petroleum hydrocarbon detection. This study proposes an innovative method for rapid in situ detection of petroleum hydrocarbons in soil, building upon the challenges highlighted in traditional methods for organic pollutant detection. Recognizing the limitations of complex sample pretreatment and the challenges posed by the diverse structures of PAHs, ranging from two rings to six or more rings, as discussed earlier, this research aims to address these issues by developing a novel experimental system with simple and fast pretreatment steps. This system does not rely on complicated instruments typically associated with traditional detection methods, such as gas chromatography and mass spectrometry. Instead, it utilizes LED (light-emitting diode (LED)) light sources and CCD detectors to offer a streamlined and efficient approach to detecting petroleum hydrocarbons in soil. By focusing on rapid in situ detection, this method aims to overcome the limitations of traditional laboratory-based techniques, offering a practical solution for monitoring soil organic pollution in real time, particularly in areas affected by oil refinery relocation. This LED has been used in several experimental studies in which artificially proportioned soil petroleum hydrocarbon samples were used to verify the correlation between petroleum hydrocarbon concentrations and fluorescence values. We also established a predictive regression model for the total amount of soil petroleum hydrocarbons present. The present research provides a practical and efficient solution to environmental monitoring and pollution control for the rapid assessment and management of soil petroleum hydrocarbon contamination, especially in areas left behind by oil refinery relocation. This innovative approach simplifies the detection process and reduces the need for expensive and complex analytical equipment.

MATERIALS AND METHODS

Fluorescence Imaging System. The soil petroleum hydrocarbon fluorescence imaging in situ monitoring system presented in this article is based on an ultraviolet-induced fluorescence imaging method and can be utilized for detecting petroleum hydrocarbons in soil in a rapid and nondestructive manner. With the assistance of ultraviolet light sources,

https://doi.org/10.1021/acsomega.4c01298
ACS Omega 2024, 9, 29350−29359

petroleum hydrocarbon pollutants in the soil are excited to produce fluorescent signals. With a CCD camera, fluorescence images can be quickly captured and analyzed. By detecting and analyzing the intensity and characteristic parameters of fluorescent signals, petroleum hydrocarbons can be detected and their concentrations can be determined. The main components of the system are the excitation light source module, the fluorescence imaging module, the main control unit, and the data processing unit. The excitation light source module emits light focused by the collimating lens and then irradiates the sample. Fluorescence emitted from the sample enters the fluorescence collection system through the refractive structure, the filter, and the camera lens. The fluorescence imaging module consists of a CCD detector, while the main control unit controls the various circuits in the system, such as the control of the drive circuits for the excitation light and imaging modules; finally, the data processing unit inverts qualitative and quantitative information about soil petroleum hydrocarbon pollution. Several petroleum pollutants, such as crude oil and various processed petroleum products like gasoline, diesel, kerosene, and hydraulic oil, are considered petroleum pollutants. A three-dimensional fluorescence spectrum of crude oil was obtained using an F-7000 fluorescence spectrophotometer and a characteristic analysis was conducted. This fluorescence spectrum is shown in Figure 2 along with the

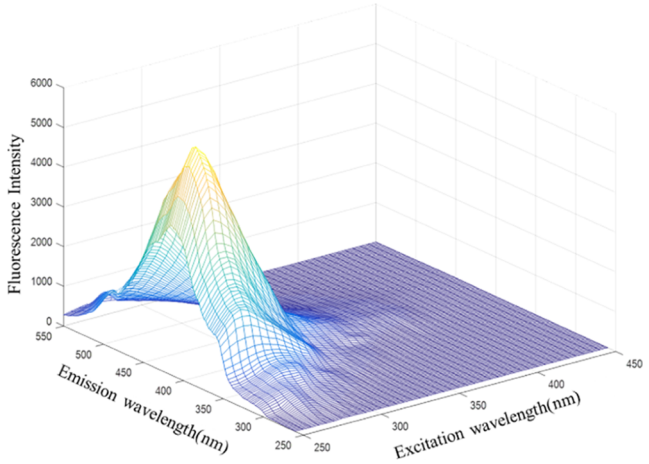

Figure 2. Crude oil three-dimensional fluorescence spectrum. The two horizontal axes are emission and excitation wavelengths respectively, and the vertical axis is fluorescence intensity value.

results of the characteristic analysis of crude oil. According to the analysis, the fluorescence peak was located between 250−350, and 260−550 nm (excitation and emission bands, respectively) in wavelength. Therefore, the light sources used in this system involve low-power-consumption, high-power, high-intensity narrow-band ultraviolet LEDs, with a wavelength of 280 nm.

In the experimental setup, ultraviolet (UV)-enhanced area array CCD cameras were used as photodetectors for detecting fluorescence, and the response range ranged between 200 and 1000 nm based on the signal length. The fluorescence signals are relatively weak, and both light sources and ambient light interfere with them. Therefore, when extracting fluorescence signals from complex backgrounds, it is necessary to effectively remove the influence of stray light before extracting fluorescence signals. We chose filters with superior performance to solve this problem. These filters were placed in front of the light source at a wavelength of 280 nm as well as in front of the camera lens to achieve the desired result. These filters will only allow the fluorescence emitted by the sample-to-be-measured to pass through and prevent all other light from passing through. In this way, excitation light at the ideal signal wavelength can be obtained while eliminating the influence of the light source and stray light. Figure 3 shows a schematic diagram.

Figure 4 shows the structural diagram of the system. The figure is the side of the instrument. It includes light source module (placed LEDs as excitation light), circuit driver module (used to control the lights on and off and drive the camera), fluorescence collection module (collects fluorescence through the beam collector), and fluorescence imaging module (used to acquire images). The light source module projects monochromatic light onto the contaminated soil, which, upon excitation by organic pollutants in the soil, generates multicolored light. This multicolored light is then projected into the fluorescence collection module and successively passes through filters and lenses before entering the fluorescence imaging module.

Sample Preparation. The standard soil selected for the experiment was the laterite soil effective component analysis standard material (NSA-6, Shaoguan, Guangdong), while the petroleum hydrocarbons used in the experiment were crude oil fractionation samples (J42002) of crude oil. The first step involved weighing a certain mass of standard soil powder and screening it through a 100-mesh sieve. A certain mass of crude oil was added to this mass of standard soil powder. Subsequently, crude oil and standard soil were thoroughly mixed and placed in a mixing machine to mix evenly. Finally, a high-concentration soil petroleum hydrocarbon sample containing 100 g/kg petroleum hydrocarbons was produced. As part of the preparation of low-concentration samples, high-concentration soil petroleum hydrocarbon samples were mixed with blank standard soil samples. The samples were stirred and ground using a grinder and then diluted to obtain 19 soil petroleum hydrocarbon samples ranging from 5 to 100 g/kg. The samples were flattened and placed in the sample box for measurement, as shown in Figure 5.

Test ability evaluation indicator. The relative standard deviation (RSD) is used as a judgment standard for calculating whether a system functions stably. It is calculated using the formula below

$$D_{\mathrm{RS}} = \frac{\sqrt{\frac{\sum_{i=1}^{n}(x_i - \overline{x})^2}{n-1}}}{\overline{x}} \quad (1)$$

where n is the number of measurements, x_i is the value for the ith time, and $\overline{x}$ is the average of n measured values. The better the system stability, the lower the RSD obtained when testing the same concentration sample multiple times.

Parameter Analysis and Data Acquisition. For data collection to take place, we must connect the CCD camera, the control system, and the computer, and start the acquisition software so that we can set the acquisition parameters. There is no doubt that light source energy plays a key role in fluorescence analysis because it directly affects the intensity of the fluorescence signal. When the light source energy is low, for instance, the fluorescence signal may be weak, especially for low-concentration samples, and the excitation effect will be poor, which is detrimental to quantitative analysis. When the light source energy is too high, the fluorescence signal may

https://doi.org/10.1021/acsomega.4c01298
ACS Omega 2024, 9, 29350−29359

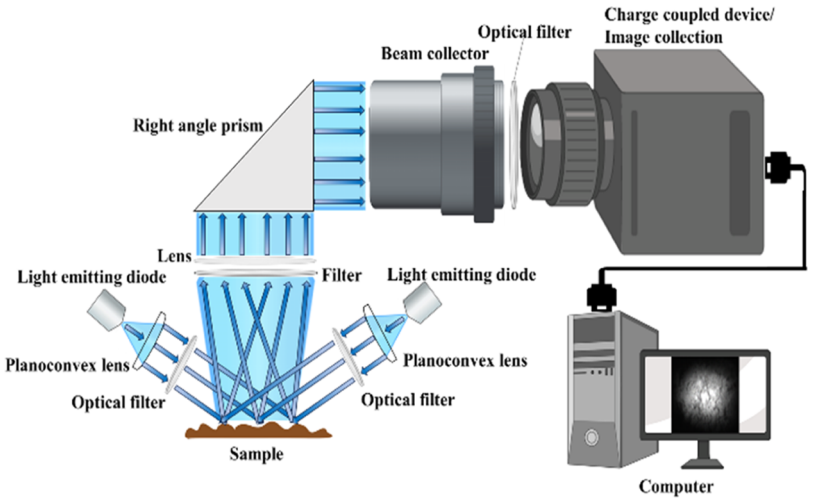

Figure 3. Imaging system schematic. It contains light-emitting diode, planoconvex lens, optical filter, right angle prism, beam collector, charge-coupled device, sample, and computer.

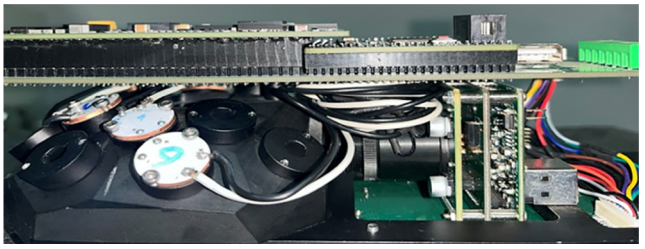

Figure 4. System structure diagram. On the side of the instrument, we can clearly see the connection between the LEDs and the circuit board, as well as the location of the camera module.

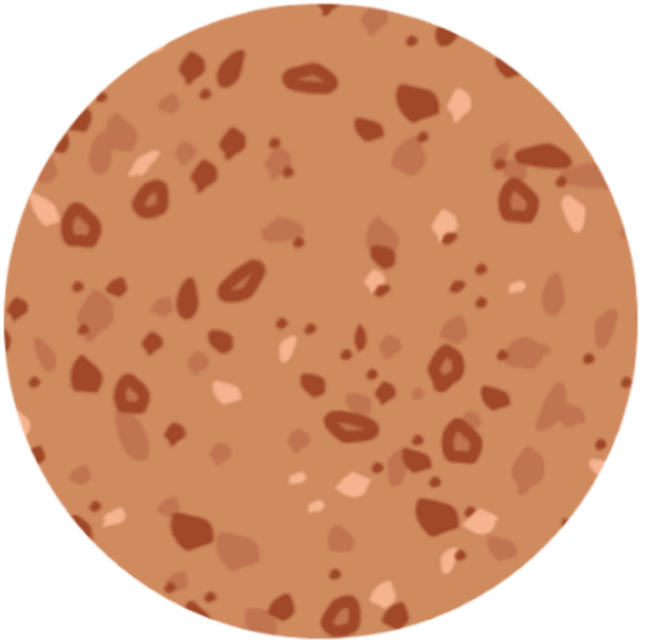

Figure 5. Soil sample. It only represents a sample of a certain concentration. The greater the concentration, the darker the color of the sample.

become saturated for high-concentration samples, which will also affect the accuracy.

Consequently, choosing the appropriate light source energy for the experiment is the key to success. First, a light source with a wavelength of 280 nm was selected as the excitation light source. Second, the light source intensity should be adjusted so that it is most effective. Finally, the camera's exposure time was adjusted, and the burst mode was set. This approach enabled us to take 10 images of each soil sample each time. The average fluorescence value of these 10 images was summed into a single value, which was used as the result for each sample. This is done to enhance the reliability. To avoid the influence of ambient light on the experimental results, black shading cloth was used for the entire experiment to shield the experimental system. These operations will help to ensure that the results are not affected by ambient light during the experiment.

Image Denoising and Fluorescence Edge Detection. During image acquisition by the CCD camera, various noises may be introduced into the image. This is due to the influence of various factors, such as sensor material properties, the working environment, the electronic components, and the circuit structure. It is also possible that the transmission and recording of image signals may also be interfered with by factors such as transmission media and recording equipment. This may contaminate digital images when they are transmitted and recorded. It has been proven that when parts of the foreground are mistakenly classified as background or when parts of the background are incorrectly classified as foreground, the difference between the two parts is reduced, increasing the probability of segmentation errors and generating noise. For this reason, two commonly used noise reduction methods are Gaussian filtering and median filtering. Noise can be reduced using both these methods. The results of Gaussian filtering and median filtering are similar after processing, as shown in Figure 6. However, the calculated signal-to-noise ratio (SNR) results show that the Gaussian filtering and median filtering SNRs are 48.66 and 41.85 dB, respectively. In general, a high SNR represents a high strength of the signal relative to the noise. Furthermore, mean filtering can easily create blurry images, especially when processing edge information and features. To obtain the optimal noise reduction effect, the Gaussian noise reduction method was chosen, and the appropriate filter size and standard deviation were selected based on the optimal

https://doi.org/10.1021/acsomega.4c01298
ACS Omega 2024, 9, 29350−29359

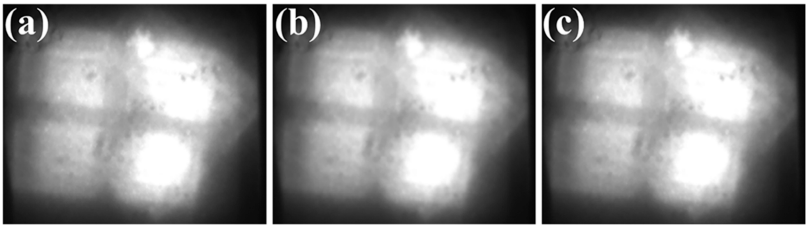

Figure 6. Processed image results of different filtering methods. (a) Image before filtering, (b) Gaussian-filtered image, and (c) mean-filtered image.

Table 1. Blank Sample Signal Value at 280 nm Excitation[a]

110 blank sample data values										
#1	#2	#3	#4	#5	#6	#7	#8	#9	#10	#11
8.04	8.04	8.03	8.04	8.03	8.01	8.01	8.01	8.01	8.01	8.00
8.04	8.02	8.02	8.02	8.02	7.99	8.00	8.00	8.00	7.99	7.99
8.02	8.03	8.02	8.02	8.02	7.99	7.99	7.99	7.99	7.98	7.98
8.08	8.00	8.01	8.00	8.00	7.98	7.98	7.97	7.92	7.98	7.98
8.08	8.00	7.99	7.99	8.00	7.98	7.98	7.97	8.10	7.97	7.97
8.05	8.02	8.03	8.03	8.02	8.02	8.02	8.02	8.02	8.01	7.99
8.03	8.01	8.01	8.01	8.02	8.00	8.00	8.00	8.01	8.01	7.98
8.02	8.00	8.00	8.01	8.01	8.00	8.00	7.99	7.99	7.98	7.98
8.02	7.98	7.99	8.00	8.00	7.99	7.98	7.99	7.99	7.97	7.97
8.00	7.99	7.99	7.99	7.98	7.98	7.98	7.98	7.98	7.96	7.96

[a]We measured 11 times for a total of 110 images and calculated the standard deviation between the corresponding signal values.

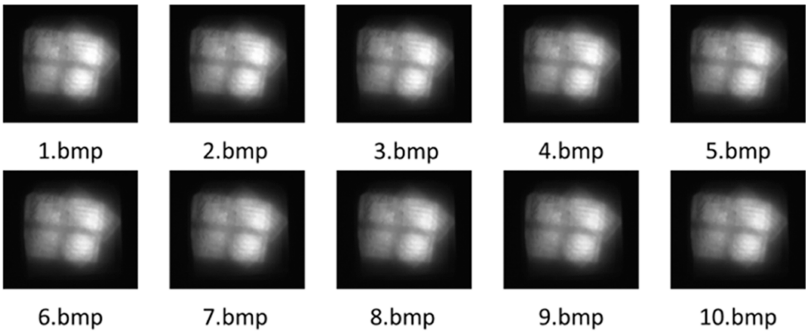

Figure 7. Fluorescence images of soil samples containing crude oil. Ten images captured of the same sample under the same exposure time and light intensity, numbered 1−10.

noise reduction effect requirement. Several experiments have shown that the most effective filtering effect can be obtained when the filter size is 5 × 5 and the standard deviation is 1.

It is necessary to denoise and smooth the image after which edge detection should be performed on the fluorescence signals in the image to obtain an appropriate threshold for binary processing of the image. The edge of an image is the most basic feature of an image because it usually exists where the grayscale changes significantly. Only when grayscale changes are apparent can the object's outline be clearly observed. In this study, we explored the Otsu algorithm,[25] and thresholds were used to divide the original image into foreground and background images. Optimal thresholds should be determined by the differences between the background and the foreground. The standard for measuring differences is variance between classes. This method is very sensitive to noise and target size. It produces better segmentation results for images with unimodal variance. A threshold τ is set to divide the pixels in the image into two categories: A ($>\tau$) and B ($<\tau$). The main principle is to count the pixels corresponding to each gray level in the image. As n_i is the number of pixels that correspond to gray level i, $n_0,n_1,n_2,\cdots,n_{255}$ will exist in the image. The probability of the pixel gray level being i is

$$p_i = \frac{n_i}{n_0 + n_1 + \cdots + n_{255}} \tag{2}$$

Now we need to find the τ that maximizes the variances of the two categories. To do this, we can traverse all integers from 0 to 255, find all of the variances that correspond to each integer, and then take the τ that corresponds to the largest variance. If the threshold is k, the probability that a pixel is assigned to A is $p_A(k)$, and the average gray level of the pixel assigned to A is $m_A(k)$. With the same probability that a pixel is assigned to B as $p_B(k)$ and that the average gray level of the pixel assigned to B is $m_B(k)$, the cumulative mean gray level k is m, and the gray value of the entire image is m_G, we have

$$p_A(k) \times m_A(k) + p_B(k) \times m_B(k) = m_G \tag{3}$$

$$p_A(k) + p_B(k) = 1 \tag{4}$$

The variance is as follows

https://doi.org/10.1021/acsomega.4c01298
ACS Omega 2024, 9, 29350−29359

Table 2. Signal Values for Different Samples[a]

concentration g/kg	signal values										sum
0	8.04	8.04	8.02	8.08	8.08	8.05	8.03	8.02	8.02	8.00	80.37
5	11.12	11.09	11.02	10.95	10.92	10.73	10.67	10.29	10.24	10.19	107.22
10	14.63	14.49	14.42	14.31	14.27	13.83	13.75	13.64	13.20	13.12	139.65
15	20.13	20.03	19.82	19.65	19.58	18.78	18.64	18.46	18.43	18.26	191.77
20	28.96	28.62	28.42	28.14	27.51	26.56	25.94	25.80	25.57	25.36	270.86
25	35.51	34.72	34.32	33.96	33.42	32.63	31.94	31.65	31.50	31.24	330.90
30	41.89	41.05	40.63	40.27	39.71	38.33	37.98	37.66	37.52	36.82	391.86
35	52.58	51.69	51.41	50.55	50.07	47.61	47.21	46.99	46.25	45.86	490.22
40	63.15	62.09	61.76	60.78	60.23	58.69	57.72	57.49	57.00	56.15	595.06
45	80.58	80.16	78.92	77.76	76.67	74.28	73.57	72.95	71.94	71.38	758.20
50	89.87	89.01	87.77	86.98	86.22	84.05	83.33	82.22	81.18	80.86	851.49
55	105.71	104.36	103.07	102.58	101.37	101.60	100.38	99.50	98.35	97.23	1014.14
60	116.18	114.71	114.19	112.78	111.44	110.77	109.96	108.65	108.23	107.01	1113.92
65	129.48	127.90	126.40	125.44	124.10	122.36	120.96	119.63	118.34	117.90	1232.52
70	137.83	135.89	134.42	133.84	132.43	132.43	131.04	129.67	129.17	127.85	1324.57
75	155.70	154.11	153.40	151.51	150.03	149.83	148.28	146.82	146.30	144.90	1500.88
80	171.01	168.85	167.13	165.48	163.80	163.99	162.39	161.45	159.87	159.33	1643.30
85	182.41	181.43	179.63	178.62	176.92	178.61	176.86	175.90	174.25	172.62	1777.24
90	192.42	190.70	190.06	187.99	186.41	188.02	186.32	184.74	183.17	181.56	1871.38
100	206.36	204.88	204.34	202.90	201.95	199.24	197.74	197.25	195.73	194.73	2005.12

[a]The first column represents the concentration values of different samples, the middle 10 columns correspond to the signal values of 10 images of each sample, and the last column represents the sum of the signal values.

$$\sigma^2 = p_A(k)(m_A(k) - m_G)^2 + p_B(k)(m_B(k) - m_G)^2 \quad (5)$$

where $p_A(k) = \sum_{i=0}^{k} p_i$ $p_B(k) = \sum_{i=k+1}^{255} p_i$

$$m = \sum_{i=0}^{k} ip_i m_G = \sum_{i=0}^{255} ip_i$$

$$m_A(k) = \frac{\sum_{i=0}^{k} ip_i}{p_A(k)}, m_B(k) = \frac{\sum_{i=k+1}^{255} ip_i}{p_B(k)}$$

in the case where the gray level k that maximizes formula (5) is determined, that is what Otsu's threshold τ is.

RESULTS AND DISCUSSION

280 nm LED Excitation. In a similar manner, an LED light source with a wavelength of 280 nm had been used to measure the blank soil petroleum hydrocarbon sample. A total of 11 sets of data had been obtained, with 10 images in each group, for a total of 110 images. A standard deviation of 0.0244 was calculated by formula (1), and its values are listed in Table 1.

After that, we used a light source of this wavelength to excite 19 soil petroleum hydrocarbon samples and obtained the image shown in Figure 7, which shows the shape of the light source due to the LED light source chip. The cumulative values of the 10 image signals were calculated, and the results are presented in Table 2. The cubic polynomial equation is fit to the image signal value: $y = -2.292 \times 10^{-12} x^3 + 4.265 \times 10^{-7} x^2 - 3.65 \times 10^{-4} x + 97.86$. Figure 8 shows the fitting curve.

The fit curve has a correlation coefficient of 0.999, and the relative error between the true concentration and the inverted concentration can also be calculated, as illustrated in Table 3. Figure 9 shows the numerical values and errors, and the relative error is within 10%.

Keeping the wavelength and various parameters unchanged, the sample was shaken, and the measurement was repeated. The experiment was performed 4 times in total. We found that the measurement results are stable. The inverted concentration of each measurement was obtained using the curve equation, and the relative error was calculated. The error fluctuates within a small range, as shown in Table 4 and Figure 10.

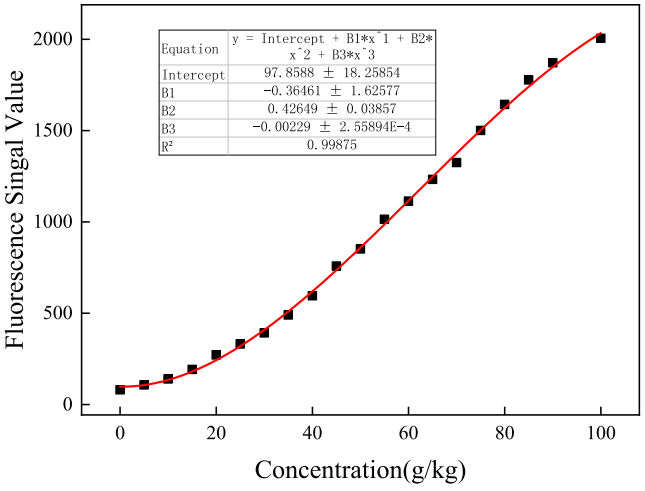

Figure 8. Fitting curve graph of samples with different concentrations. We use all of the points to perform cubic curve fitting and establish an inversion model. The abscissa represents the concentration, and the ordinate represents the signal value.

Field Studies and Results. The fluorescence imaging in situ monitoring system has been used to conduct field experiments at an abandoned oil storage area in Anqing City, Anhui Province, in April 2023. The total amount of petroleum hydrocarbons in the soil profile was obtained in real time, and the stability and reliability of the system operation were evaluated. As the demonstration site was originally an oil storage facility in Anqing, the oil tanks were dismantled in 2010. The site is currently undergoing soil restoration and reconstruction. Because crude oil has been stored for a long period of time in large quantities, there is a risk of

https://doi.org/10.1021/acsomega.4c01298
ACS Omega 2024, 9, 29350−29359

Table 3. True Values, Inverted Values, and Relative Errors of Samples with Different Concentrations[a]

true value g/kg	inverted value g/kg	relative error (%)	true value g/kg	inverted value g/kg	relative error (%)
5	5.21	4.2	55	56.07	1.9
10	10.66	6.6	60	59.91	0.2
15	16.00	6.7	65	64.46	0.8
20	21.93	9.7	70	68.00	2.9
25	25.68	2.7	75	74.93	0.1
30	29.10	3.0	80	80.78	1.0
35	34.09	2.6	85	86.65	1.9
40	38.94	2.7	90	91.11	1.2
45	45.91	2.0	100	98.25	1.8
50	49.69	0.6			

[a]We used all of the 19 samples to invert the concentration and calculated the error between it and the actual concentration.

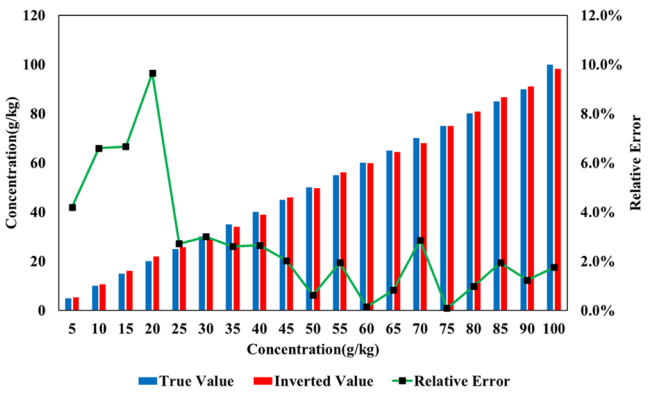

Figure 9. True values, inverted values, and relative errors between them. We visually display the actual concentration, inverted concentration and error values using bar graphs and dot-line graphs, respectively.

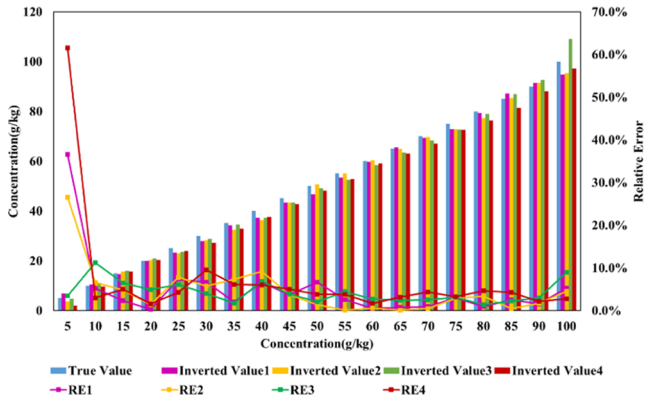

Figure 10. Comparison of results from four repeated experiments. We visually display the actual concentration, inverted concentration, and error values using bar graphs and dot-line graphs, respectively.

contamination, so this area has been chosen as an off-site testing facility. In accordance with the site conditions, six monitoring points were established horizontally. A hole with a depth of 100 cm and a diameter of 11 cm was drilled at each point to detect the top layer (30 cm), the middle layer (60 cm), and the bottom layer (90 cm) of the soil. To prepare the soil for testing, we measured the physical and chemical characteristics of the soil. The pH of the soil was 7.5, and the humidity was 20%. Figure 11 illustrates the location layout of the venue.

We used our monitoring system to obtain real-time fluorescence images of petroleum hydrocarbon pollution at each profile monitoring point and inverted the concentration. The power supply voltage was direct current 24 V, and the detector exposure time was 79.5 ms. There were 18 data sets collected during the field experiment. Figure 12 shows the distribution results of petroleum hydrocarbon concentrations in the soil. The analysis revealed that the distributions of petroleum hydrocarbon contamination in the profiles at the six

Table 4. True Value, Inverted Value, and Relative Errors for Four Repeated Experiments[a]

true value g/kg	inverted value g/kg	RE1 (%)	inverted value g/kg	RE2 (%)	inverted value g/kg	RE3 (%)	inverted value g/kg	RE4 (%)
5	6.83	36.6	3.67	26.6	4.83	3.4	1.92	61.6
10	10.52	5.2	10.66	6.6	11.12	11.2	9.70	3.0
15	14.65	2.3	15.72	4.8	15.97	6.5	15.75	5.0
20	20.05	0.3	20.28	1.4	20.98	4.9	20.31	1.5
25	23.17	7.3	23.06	7.8	23.48	6.1	23.94	4.2
30	28.00	6.7	28.28	5.7	28.80	4.0	27.13	9.6
35	34.28	2.1	32.44	7.3	34.38	1.8	32.86	6.1
40	37.36	6.6	36.34	9.1	37.27	6.8	37.60	6.0
45	43.35	3.7	43.35	3.7	43.26	3.9	42.74	5.0
50	46.67	6.7	50.69	1.4	49.00	2.0	48.09	3.8
55	53.56	2.6	55.06	0.1	52.55	4.5	52.91	3.8
60	59.73	0.5	60.32	0.5	58.39	2.7	58.99	1.7
65	65.48	0.7	64.96	0.1	63.41	2.4	62.93	3.2
70	69.33	1.0	69.66	0.5	68.27	2.5	66.92	4.4
75	72. 79	2.9	72.82	2.9	72.69	3.1	72.55	3.3
80	79.29	0.9	77.33	3.3	78.86	1.4	76.30	4.6
85	87.09	2.5	85.43	0.5	86.93	2.3	81.39	4.2
90	91.41	1.6	91.48	1.6	92.64	2.9	88.12	2.1
100	94.76	5.2	95.42	4.6	108.97	9.0	97.26	2.7

[a]We used all of the 19 samples to invert the concentration and calculated the error between it and the actual concentration. The relative errors are represented by RE1, RE2, RE3, and RE4, respectively.

https://doi.org/10.1021/acsomega.4c01298
ACS Omega 2024, 9, 29350−29359

Figure 11. Venue location layout. We found these 6 points in the abandoned oil storage area, numbered 1−6, and marked them on the satellite map, and then took 3 soil samples at different depths from each point (Map data ©2022 Google).

monitoring points are similar. As the depth increases, the concentration of petroleum hydrocarbons increases as well.

In the field experiment, the system operated without malfunction, and the hardware and software both operated smoothly. Eighteen data sets were collected, each containing 10 data points. The RSDs of the 18 groups of data are shown in Figure 13. The RSD values of 16 of the 18 groups were all less than 1%. The RSD values of the two remaining groups were slightly greater, at 2.89 and 5.02%, respectively. These results suggest that the measurement results are highly stable.

The application of fluorescence imaging technology for organic pollutant detection overcomes the shortcomings of traditional organic matter detection methods, such as the complexity of sample preparation and slow testing speed, and has the characteristics of rapid detection and ease of use. A self-developed soil organic pollutant fluorescence imaging in situ monitoring system is developed in this article to analyze the impact of fluorescence signals produced by soil petroleum hydrocarbons under 280 nm wavelength of LED excitation. Its

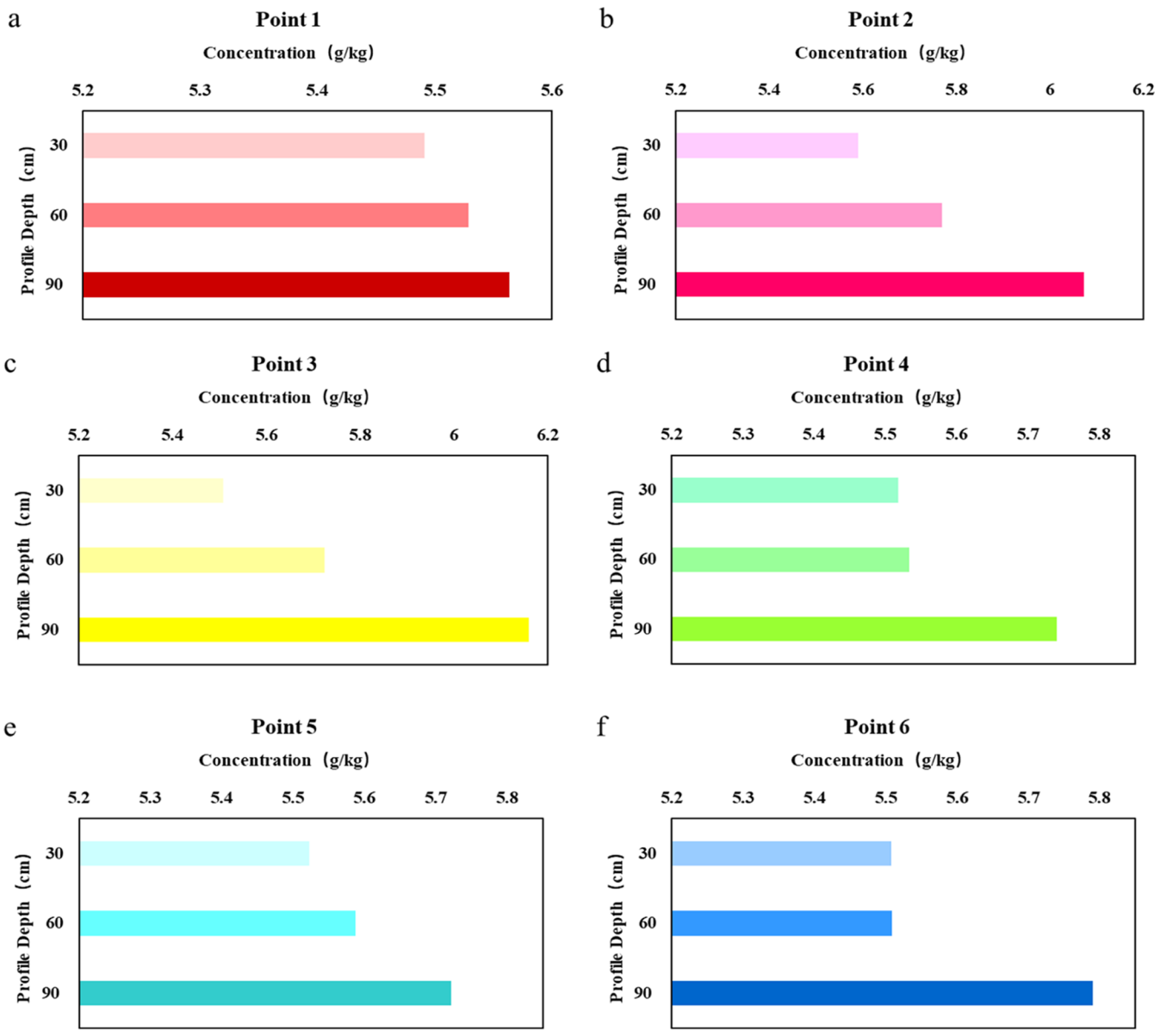

Figure 12. Soil petroleum hydrocarbon concentration distribution. Panels (a−f) correspond to points 1−6 in Figure 11.

https://doi.org/10.1021/acsomega.4c01298
ACS Omega 2024, 9, 29350−29359

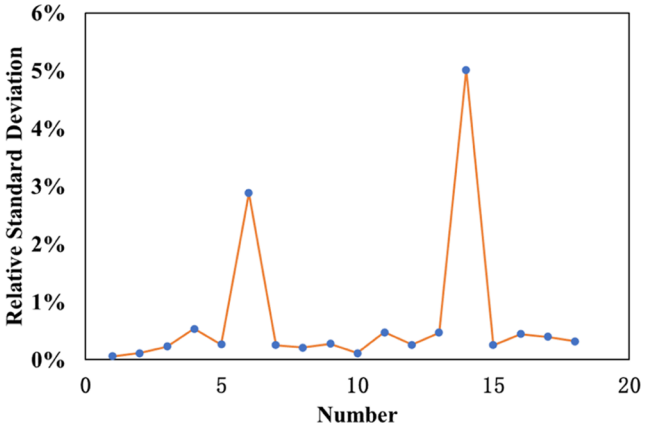

Figure 13. RSDs of 18 sets of data. We calculate the relative standard deviation of the signal values of 10 images in each group.

precision and accuracy ensure rapid detection on the ground. The purpose of this study was to provide a methodological basis for using fluorescence imaging in situ monitoring technology to monitor soil petroleum aromatic hydrocarbon organic contamination in a rapid and efficient manner. Additionally, the monitoring system was applied to a waste oil storage area and no faults were detected during operation, indicating that the measurement results are highly reliable when applied on site. In the following research and development work, an upgrade of the system is planned, including increasing the number of LED light sources to increase the energy of the excitation light source and examining the effects of LED light sources of different wavelengths on the acquisition and calibration curves of soil petroleum hydrocarbons at lower concentrations. Additionally, the impact of physical and chemical parameters such as soil moisture and organic matter will be explored to improve the system's performance and accuracy.

■ ASSOCIATED CONTENT

Supporting Information

The Supporting Information is available free of charge at https://pubs.acs.org/doi/10.1021/acsomega.4c01298.

Properties of standard soil (Table S1) (PDF)

■ AUTHOR INFORMATION

Corresponding Authors

Ruifang Yang − *Key Laboratory of Environmental Optics and Technology, Anhui Institute of Optics and Fine Mechanics, Chinese Academy of Sciences, Hefei 230031, China; Key Laboratory of Optical Monitoring Technology for Environment of Anhui Province, Hefei 230031, China*; Email: rfyang@aiofm.ac.cn

Nanjing Zhao − *Key Laboratory of Environmental Optics and Technology, Anhui Institute of Optics and Fine Mechanics, Chinese Academy of Sciences, Hefei 230031, China; Key Laboratory of Optical Monitoring Technology for Environment of Anhui Province, Hefei 230031, China*; Email: njzhao@aiofm.ac.cn

Authors

Gaoyong Shi − *College of Environmental Science and Optoelectronic Technology, University of Science and Technology of China, Hefei 230026, China; Key Laboratory of Environmental Optics and Technology, Anhui Institute of Optics and Fine Mechanics, Chinese Academy of Sciences, Hefei 230031, China; Key Laboratory of Optical Monitoring Technology for Environment of Anhui Province, Hefei 230031, China*; orcid.org/0009-0006-3709-6570

Gaofang Yin − *Key Laboratory of Environmental Optics and Technology, Anhui Institute of Optics and Fine Mechanics, Chinese Academy of Sciences, Hefei 230031, China; Key Laboratory of Optical Monitoring Technology for Environment of Anhui Province, Hefei 230031, China*

Jinqiang Yang − *Key Laboratory of Environmental Optics and Technology, Anhui Institute of Optics and Fine Mechanics, Chinese Academy of Sciences, Hefei 230031, China; Key Laboratory of Optical Monitoring Technology for Environment of Anhui Province, Hefei 230031, China; Science Island Branch, Graduate School of USTC, Hefei 230026, China*

Yuxi Jiang − *Key Laboratory of Environmental Optics and Technology, Anhui Institute of Optics and Fine Mechanics, Chinese Academy of Sciences, Hefei 230031, China; Key Laboratory of Optical Monitoring Technology for Environment of Anhui Province, Hefei 230031, China; Science Island Branch, Graduate School of USTC, Hefei 230026, China*

Wenqing Liu − *Key Laboratory of Environmental Optics and Technology, Anhui Institute of Optics and Fine Mechanics, Chinese Academy of Sciences, Hefei 230031, China; Key Laboratory of Optical Monitoring Technology for Environment of Anhui Province, Hefei 230031, China*

Complete contact information is available at: https://pubs.acs.org/10.1021/acsomega.4c01298

Author Contributions

G.S.: data curation, writing—original draft; R.Y.: review and editing; N.Z.: conceptualization and approval of the final version; G.Y., J.Y., Y.J., and W.L.: suggestions

Notes

The authors declare no competing financial interest.

■ ACKNOWLEDGMENTS

This research was performed with financial support from the Key Technologies Research and Development Program (CN) Nos. 2022YFC3700902, 2020YFC1807204-1; the Science and Technology Service Network Initiative (CN) No. KFJ-STS-QYZD-2021-04-001-4; and the Director's Fund Project of Hefei Institute (YZJJ2023QN09).

■ REFERENCES

(1) Fan, Y.; Wang, X.; Funk, T.; Rashid, I.; Herman, B.; Bompoti, N.; Mahmud, M.S.; Chrysochoou, M.; Yang, M.; Vadas, T. M.; LEI, Y.; LI, B. A Critical Review for Real-Time Continuous Soil Monitoring: Advantages, Challenges, and Perspectives. *Environ. Sci. Technol.* **2022**, *56* (19), 13546−13564, DOI: 10.1021/acs.est.2c03562.

(2) Ogbunuzor, C. C.; Hellier, P. R.; Talibi, M.; Ladommatos, N. In-Cylinder Polycyclic Aromatic Hydrocarbons Sampled during Diesel Engine Combustion. *Environ. Sci. Technol.* **2021**, *55* (1), 571−580, DOI: 10.1021/acs.est.0c05561.

(3) Humel, S.; Schmidt, S. N.; Sumetzberger-Hasinger, M.; Mayer, P.; Loibner, A. P. Enhanced Accessibility of Polycyclic Aromatic Hydrocarbons (PAHs) and Heterocyclic PAHs in Industrially Contaminated Soil after Passive Dosing of a Competitive Sorbate.

Environ. Sci. Technol. **2017**, *51* (14), 8017−8026, DOI: 10.1021/acs.est.7b01198.
(4) Dong, W. Case study of the exhaust gas treatment during soil remediation at the original sites of petrochemical enterprises. *Pet. Process. Petrochem.* **2021**, *52* (06), 112−116.
(5) Xuhao, Z. Environmental Investigation of Soil and Groundwater on the Relocation Site of a Gas Station in Shanghai. *Constr. Des. Eng.* **2020**, No. 16, 129−131.
(6) Yueya, C. Contamination investigation and characteristics analysis of the pickling site in a mechanical processing factory in Shijiazhuang City. *Environ. Dev.* **2020**, *32* (04), 19−21.
(7) Yige, D.; Xin, L.; Aiguo, Z.; Ranqiong, W.; Jianwei, B. A new model for treating oil-polluted farmland. *Anhui Agric. Sci.* **2013**, *41* (06), 2626−2628.
(8) Chakravarty, P.; Deka, H. Enzymatic defense of Cyperus brevifolius in hydrocarbons stress environment and changes in soil properties. *Sci. Rep.* **2021**, *11*, No. 718, DOI: 10.1038/s41598-020-80854-5.
(9) Chen, Y.; Zhang, J.; Zhang, F.; Liu, X.; Zhou, M. Contamination and health risk assessment of PAHs in farmland soils of the Yinma River Basin, China. *Ecotoxicol. Environ. Saf.* **2018**, *156*, 383−390, DOI: 10.1016/j.ecoenv.2018.03.020.
(10) Chen, X.; Li, L.; Zhang, Y.; Gu, H. Microwave Heating Remediation of Light and Heavy Crude Oil-Contaminated Soil. *Energy Fuels* **2023**, *37* (7), 5323−5330, DOI: 10.1021/acs.energyfuels.3c00078.
(11) Kim, Y.-Y.; Kim, M.-K.; HanSeung, H.-S. Determination of volatile organic compounds (VOCs) levels from various smoking cessation aids by using gas chromatography-mass spectrometry methodology. *J. Toxicol. Environ. Health, Part A* **2021**, *85* (3), 110−120, DOI: 10.1080/15287394.2021.1979436.
(12) Halder, S.; Xie, Z.; Nantz, M. H.; Fu, X.-A. Integration of a micropreconcentrator with solid-phase microextraction for analysis of trace volatile organic compounds by gas chromatography-mass spectrometry. *J. Chromatogr. A* **2022**, *1673*, No. 463083, DOI: 10.1016/j.chroma.2022.463083.
(13) Guosheng, C.; Shaohan, W.; YueMei, C.; Haozhi, X.; Hua, X.; Tao, C.; Ludan, Y.; Houjin, L.; Fang, Z.; Gangfeng, O. Y. Rapid determination of trace benzene series in water by solid phase microextraction combined with gas chromatography-mass spectrometry. *Coll. Chem.* **2022**, *37* (05), 76−83.
(14) Ledesma, L.; Boschetti, B.; Martion, M.; Bortolato, B. Application of thymine-based copolymers in the quantification of organic pollutants in water by sensitized fluorescence. *Microchem. J.* **2020**, *155*, No. 104625, DOI: 10.1016/j.microc.2020.104625.
(15) Li, T.; Cao, X.; Zhang, M. An accelerated solvent extraction and gas chromatography-flame ionization detector method to rapidly determining and assessing total petroleum hydrocarbon contamination in soil from Fushan oilfield, China. *Environ. Sci. Pollut. Res.* **2020**, *27* (30), 37444−37454, DOI: 10.1007/s11356-020-09418-4.
(16) Hawthorne, S. B.; Grabanski, C. B. Correlating Selective Supercritical Fluid Extraction with Bioremediation Behavior of PAHs in a Field Treatment Plot. *Environ. Sci. Technol.* **2000**, *34* (19), 4103−4110, DOI: 10.1021/es001178o.
(17) Sim, W.; Choi, S.; Lee, H.-J.; kim, K.; Park, K.; Oh, J.-E. Evaluation of sample preparation methods for suspect and non-target screening in water, sediment, and biota samples using gas chromatography coupled to high-resolution mass spectrometry. *Sci. Total Environ.* **2022**, *849*, No. 157835, DOI: 10.1016/j.scitotenv.2022.157835.
(18) Yan-hong, G.; Zhao-lu, Z.; Zhen-zhen, Z.; Chao-yi, S.; Xian-he, G.; Jun, L. Algorithmic study of total petroleum hydrocarbons in contaminated soil by three-dimensional excitation-emission matrix fluorescence spectroscopy. *Chin. Opt.* **2020**, *13* (4), 852−864, DOI: 10.37188/CO.2019-0216.
(19) Wen-qi, Y.; Zhi-li, C.; Yu-wei, J.; Hong-tao, L.; Qiang, L. Research on visible-near infrared spectral characterization of purplish soil contaminated with petroleum hydrocarbon and estimation of pollutant content. *Spectrosc. Spectral Anal.* **2017**, *37* (12), 3924−3931.
(20) Wu, M.; Lin, N.; Li, G.; Liu, H.; Li, D. Hyperspectral estimation of petroleum hydrocarbon content in soil using ensemble learning method and LASSO feature extraction. *Environ. Pollut. Bioavailability* **2022**, *34* (1), 308−320, DOI: 10.1080/26395940.2022.2102543.
(21) Hao, J.; Dong, F.; Li, Y.; Wang, S.; Cui, J.; Liu, S.; Lv, Y. Quantification of polycyclic aromatic hydrocarbons in roasted Tan lamb using fluorescence hyperspectral imaging technology. *J. Food Compos. Anal.* **2023**, *124*, No. 105646, DOI: 10.1016/j.jfca.2023.105646.
(22) Qazi, F.; Shahsavari, E.; Prawer, S.; Ball, A. S.; omljenovic-Hanic, S. Detection and identification of polyaromatic hydrocarbons (PAHs) contamination in soil using intrinsic fluorescence. *Environ. Pollut.* **2021**, *272*, No. 116010, DOI: 10.1016/j.envpol.2020.116010.
(23) McCall, W.; Christy, T. M.; Pipp, D. A.; Jaster, B.; et al. Evaluation and application of the optical image profiler (OIP) a direct push probe for photo-logging UV-induced fluorescence of petroleum hydrocarbons. *Environ. Earth Sci.* **2018**, *77*, No. 374, DOI: 10.1007/s12665-018-7442-2.
(24) Cao, S.; Zhan, G.; Wei, K.; Zhou, B.; Zhang, H.; Gao, T.; Zhang, L. Raman spectroscopic and microscopic monitoring of on-site and in-situ remediation dynamics in petroleum contaminated soil and groundwater. *Water Res.* **2023**, *233*, No. 119777, DOI: 10.1016/j.watres.2023.119777.
(25) Wisaeng, K.; Sa-ngiamvibool, W. ; Brain Tumor Segmentation Using Fuzzy Otsu Threshold Morphological Algorithm. *IAENG International Journal of Applied Mathematics*. 2023, *53* (2).

https://doi.org/10.1021/acsomega.4c01298
ACS Omega 2024, 9, 29350−29359